

# Performance of the Optical Communication Adaptive Optics Testbed

Mitchell Troy<sup>a</sup>, Jennifer Roberts<sup>a</sup>, Steve Guiwits<sup>a</sup>, Steve Azevedo<sup>a</sup>, Siddarayappa Bikkannavar<sup>a</sup>, Gary Brack<sup>a</sup>, Vachik Garkanian<sup>a</sup>, Dean Palmer<sup>a</sup>, Benjamin Platt<sup>a</sup>, Tuan Truong<sup>a</sup>, Kent Wallace<sup>a</sup>, Keith Wilson<sup>a</sup>

<sup>a</sup>Jet Propulsion Laboratory, California Institute of Technology

## ABSTRACT

We describe the current performance of an adaptive optics testbed for optical communication. This adaptive optics system allows for simulation of night and day-time observing on a 1 meter telescope with a 97 actuator deformable mirror. In-lab-generated seeing of 2.1 arcseconds (at 0.5  $\mu\text{m}$ ) the system achieves a Strehl of 21% at 1.064  $\mu\text{m}$  (210 nm RMS wavefront). Predictions of the system's performance based on real-time wavefront sensor telemetry data and analytical equations are shown to agree with the observed image performance.

Keywords: Adaptive optics, telescopes, optical communication

## 1. INTRODUCTION

The Optical Communication testbed is an adaptive optics (AO) system, designed and built at the Jet Propulsion Laboratory, that measures and corrects for simulated atmospheric turbulence in the path of an optical communications signal. The significance of measured improvements in the communications signal through the use of AO is dependent on a thorough understanding of AO system performance. Performance of an AO system can be characterized in many ways; in this paper we analyze the performance in terms of the mean-squared wavefront error ( $\sigma^2$ ) which is a sum of individual, independent error terms ( $\sigma_i$ ). In this analysis, error terms are decomposed into atmospheric fitting error, temporal errors from the deformable and tip/tilt mirror, as well as calibration errors. The AO telemetry system produced data for the performance analysis. A comparison of the predicted performance with the experimental results demonstrates good agreement.

The testbed description, given in section 2, includes information on the turbulence generator, deformable mirror, and optical path. Section 3 presents experimental results from open and closed loop AO system performance, along with a description of plate scale measurements. Section 4 predicts the AO system performance considering spatial and temporal turbulence statistics, tip/tilt errors, high order temporal errors, atmospheric errors, and calibration error. We conclude with a comparison of predicted performance with experimental results.

## 2. TESTBED DESCRIPTION

The purpose of the testbed is to measure and correct for simulated atmospheric turbulence in the path of an optical communications signal. To this end, two wavelengths (1.064  $\mu\text{m}$  and 635 nm) propagate through the system. One (635 nm) is used to measure and correct for the turbulence; the other (1.064  $\mu\text{m}$ ) will be used to send data.

Sources are injected via single mode fibers into collimating assemblies. The collimated beams are sent along the same path to the beam expander which consists of an achromatic lens and an off-axis parabola (OAP). The expanded beam size was chosen to overfill the clear aperture of the deformable mirror.

The beams pass through a turbulence generator, which was custom designed and built at JPL to simulate the atmospheric conditions expected at the JPL Optical Communications Telescope Laboratory in Wrightwood CA, the ultimate location of the testbed. In the turbulence generator, four strip heaters are bolted to the bottom surface of an

aluminum sheet. Another sheet of aluminum, perforated with 0.5 cm diameter holes spaced on a 1cm grid is attached to the top of the sheet. The purpose of this top plate is to introduce uniform columns of heated air to the optical path.

The beams then reflect off the deformable mirror (DM). The DM, manufactured by Xinetics Corporation, consists of 97 actuators on a 7-mm grid spacing. The full diameter of the mirror contains 11 actuators. Each actuator has a full stroke of 4  $\mu\text{m}$ . The DM acts as the stop in the system and limits the beam size to 70 mm. The DM electronics were built by JPL and have a bandwidth of 5 KHz, significantly larger than the 2 KHz frame rate so that no significant delay is created by the electronics.

The beam is compressed to 13.8 mm by optics identical to the expansion optics) which image the pupil (DM) onto the fast steering mirror (FSM). The FSM has a physical range of  $\pm 1$  mrad and provides tip/tilt correction.

The beam is then separated into its component wavelengths by a dichroic beam splitter. The 635 nm light continues to the wavefront sensor (WFS). The WFS consists of a lenslet array, field flattening lens, relay lens and the CCD camera. A beam compressor images the DM onto the lenslet array and reduces the beam size to match the DM actuator spacing to the pitch of the lenslet array. The relay lens matches the grid of spots to the pixels of the CCD in order to implement quad cell centroiding. The CCD is an 80x80 pixel EEV39<sup>1</sup>. We use only the center 40x40 pixels, which are binned on chip down to 20x20 (2x2 pixels per subaperture). The camera runs at speeds up to 2.1 KHz with a read noise of 6.4 electrons. When slowed below 450 Hz, read noise drops to 3.7 electrons.

Along the communications path, the 1.064  $\mu\text{m}$  beam is reduced further and focused onto the detector using a zoom lens. The zoom lens allows simulation of different detector sizes by changing the size of the focused spot. A portion of the light is split off to an imaging CCD. This allows monitoring of the beam quality and AO system performance. An integrating sphere injects background noise into the signal to simulate different background noise conditions.

Elements along the communications path are not measured by the WFS, preventing wavefront error correction. Similarly, wavefront errors in the WFS path are measured and corrected, but that correction may increase wavefront error along the communications path. These are the non-common path errors. Since the goal is to improve the optical quality along the communications path, these static wavefront errors must be calibrated out to give the best spot on the imaging camera. See section 4.4 for further discussion of these error terms.

The control software, user interface, and computer systems are a modified copy of the versions used on the Palomar AO system<sup>2</sup>. This system takes the pixel data from the WFS, calculates centroids, reconstructs the wavefront (via a matrix multiply with a reconstructor matrix) and implements a servo loop before sending commands to the DM and FSM. The real-time system can run at up to 2,000 frames per second. With a 2 KHz frame rate we expect a closed loop bandwidth of about 80Hz, the same values achieved on a similar AO system at the Palomar Hale telescope. In addition, the computer system can record real-time telemetry data at rates up to 400Hz. The 400 Hz telemetry rate is important to allow analysis of the AO system performance. This data includes the centroid position, centroid flux, reconstructed wavefront, DM actuator positions and FSM positions.

### **3. EXPERIMENTAL RESULTS**

#### **3.1. Results**

For all experimental data presented here, the AO system used a reconstructor generated with A++ and ran at a frame rate of 2000 Hz. Image data was collected using the imaging CCD on the communications path (1.064  $\mu\text{m}$ ). Each image is the background subtracted average of 200 frames; giving an approximate integration time of 15 seconds. Data were first taken under nominal lab conditions to establish the baseline wavefront error. The turbulence generator was then set to 230°C and temperature was allowed to stabilize. The resulting open and closed loop images are shown in Figure 3, plotted on a log scale. Bit error rate data for the communications signal was collected concurrently, as described in<sup>3</sup>.

The Strehl ratio (the ratio of peak intensities in the aberrated and ideal point spread functions) is used to determine the improvement in beam quality produced by the AO system. To calculate the Strehl ratio, diffraction limited Airy images

were generated using the plate scale (see section 3.2) for each specific zoom setting and the calculated center of the measured spot. These were compared to the normalized image data to obtain the Strehl ratio.

Data were collected at different zoom settings for both nominal and turbulated conditions. Figure 4 shows measured

Strehl ratios converted to wavefront error using the Marechal<sup>4</sup> approximation  $S = e^{-\left(2\pi\left(\frac{WFE}{\lambda}\right)\right)^2} = e^{-\sigma^2}$ . Baseline data for zoom setting 2 was removed due to saturation in the images. The wavefront error associated with the AO system is really just the increase in wavefront error between the closed loop with turbulence wavefront error (cl\_wfe) and the wavefront error without turbulence (static\_wfe). We call this the relative AO system performance; it is calculated by taking the quadrature difference, which is  $\sqrt{cl\_wfe^2 - static\_wfe^2}$ . The graph shows that the AO system corrects all but about 100 nm of the turbulence-induced WFE. These measurements were performed before a manual calibration of the system, as described in section 4.4. The manual calibration points shown on the graph represent the optimal baseline WFE of the system.

### 3.2. System plate scale measurements

The plate scale of the system gives the relationship between the angle of tilt in the incoming beam and spot movement at the detector. For the purpose of determining plate scale, the system acts as if the 70mm beam travels through a single powered element with a system focal length (SFL) that preserves the final F/# of the system. Therefore the plate scale is:  $\Delta\text{tilt angle} / \Delta\text{spot position} = 1/\text{SFL}$ . The SFL is determined by the output focal length and the total magnification in the system (shown in Figure 5). In our system the  $\text{SFL} = (5.08 * 5 * \text{zoom magnification}) * 164 \text{ mm}$ .

As a check on these calculations, Airy images were generated using the calculated plate scale for each zoom setting. If the calculated plate scale were correct, the Airy rings would be located at the same place in theoretical and measured images, although aberrations in the real system will make the rings less distinct. A scaling error appeared when theoretical images were compared to data taken at each zoom setting (Figure 6). By adjusting the plate scales used to generate the Airy images, the Airy pattern in the generated data was matched to the pattern in the measured data. It was determined that the required adjustments gave an average difference of 8% in the plate scale.

Zoom Setting	Real Mag	Analytical System FI	Analytical Plate Scale (arcsec/mm) (70mm beam)	Measured Plate Scale (arcsec/mm) (70mm beam)
1	0.75	3124.20	66.02	71.42
2	1.5	6248.40	33.01	35.71
3	2.25	9372.60	22.01	23.80
4	3	12496.80	16.51	17.85
5	3.75	15621.00	13.20	14.28
6	4.5	18745.20	11.00	11.90
7	5.25	21869.40	9.43	10.20

**Table 1. Calculated plate scales**

This discrepancy could be due to a cumulative effect of slight variations in the focal length or magnification of the zoom lens and magnification of the beam compressor. Based on these results, the measured plate scales are used for all subsequent calculations, including Strehl ratio and  $r_0$ .

## 4. ANALYSIS OF AO SYSTEM PERFORMANCE

The performance of an AO system can be characterized in many ways; in this section we analyze the performance in terms of the mean-squared wavefront error ( $\sigma^2$ ) which is a sum of individual error terms ( $\sigma_i$ ). Data from the AO

telemetry system (as described in section 2) is used in the following analysis. Although the camera frame rate is 2000 Hz, every 20<sup>th</sup> frame was recorded, reducing the effective frequency of the telemetry data to 100 Hz.

In the section 4.1.1 below we analyze the turbulence statistics provided by the turbulence generator described in section 2 above. In the sections below we decompose error terms into temporal errors, calibration errors, and atmospheric fitting error terms arising from the inability to correct spatial frequencies smaller than the actuator spacing. The signal in the wavefront sensor was large compared with CCD read noise allow us to ignore measurement error in the analysis. We finally bring all the error terms together and compare the predicted performance to the experimental results from section 3.

#### 4.1. Turbulence statistics

Atmospheric turbulence can be thought of as having both spatial and temporal characteristics. As will be shown below both of these characteristics significantly impact the performance of the AO system, although all too often only the spatial characteristics are considered.

##### 4.1.1. Spatial Characteristics

The atmospheric coherence length (referred to as the Fried parameter<sup>5</sup>) can be used to describe the spatial characteristics of the turbulence. The Fried parameter, denoted as  $r_0$ , is the diameter of a circle that encloses 1 radian-squared of wavefront error. Equivalently, an uncompensated long exposure image will have an angular full-width half maximum of  $\theta = \lambda/r_0$ , the observing wavelength divided by  $r_0$ . The Fried parameter is usually quoted at 0.5  $\mu\text{m}$  unless stated otherwise and depends on wavelength as  $\lambda^{6/5}$ . From the open loop image (Section 3.1) an  $r_0$  in the 70 mm beam of 8.6 mm at 1.064  $\mu\text{m}$  is estimated. The optical communication testbed simulates the performance on a 1 meter telescope. So, the  $r_0$  for a 1 meter telescope would be 12.3 cm (at 1.064  $\mu\text{m}$ ) or 5.0 cm (at 0.5  $\mu\text{m}$ ). This is equivalent to 2.1 arcsecond seeing; fairly poor conditions for astronomical sites at night, but typical for day-time observations at the OCTL<sup>6</sup>.

##### 4.1.2. Temporal Characteristics

The rate at which the AO system needs to measure and correct the wavefront is dictated by the speed at which atmospheric turbulence changes. One way to characterize the temporal characteristics is to measure the turbulence weighted wind velocity ( $v$ ). Figure 7 shows a plot of the open loop tip/tilt power spectral density (PSD), calculated from the wavefront sensor telemetry with AO control loops turned off. Atmospheric theory predicts that a change in slope should occur at  $v/D$  ( $D$  is the diameter of the telescope). Figure 7 shows a change in slope at 1 Hz, implying a wind velocity of  $\sim 1$  m/s. This result reveals a limitation in the turbulence generator, since mean wind velocities during operation are 10-15 m/s at astronomical sites<sup>7</sup>. In order to increase the wind velocity generated in the testbed, fans have been added to the turbulence generator and turbulence statistics will be retested in the future.

#### 4.2. Temporal errors

The finite time required to measure the atmospheric wavefront and apply the correction to the appropriate control device (deformable or fast steering mirror) contributes to the residual wavefront error in the AO system. Below we calculate the theoretical values for both tip/tilt and high order (all modes besides tip/tilt) corrections.

##### 4.2.1. Tip/Tilt temporal errors

The two-axis residual tip/tilt error (in radians) from the finite bandwidth of an AO system is given by<sup>8</sup>:

$$\sigma_{\text{Temporal\_TT}} = \sqrt{2} \left( \frac{f_t}{f_{3dB}} \right) \left( \frac{\lambda}{D} \right) [\text{rad}],$$

Where  $f_{3dB}$  is the -3dB point of the servo bandwidth and  $f_t$  is fundamental tracking frequency which can be approximated by:

$$f_t = 0.0811 \left( \frac{r_0}{D} \right)^{\frac{1}{6}} \left( \frac{v}{r_0} \right) [Hz]$$

The servo bandwidth (Figure 7) is ~10 Hz; approximately 10 times lower than the expected servo bandwidth. A typical servo bandwidth is 20 times lower than the wavefront sensor frame rate. This would correspond to ~100 Hz for our 2000 Hz frame rate. We believe that the lower than expected values are due to non-optimal servo control parameters. However, the wind velocity generated in the turbulator was also approximately a factor of 10 lower than the expected value in the field (Section 4.1.2), resulting in a tracking frequency 10 times lower than expected in the field. Thus in the calculation of tip/tilt temporal errors, the lower than expected tracking frequency cancels out the lower than expected servo bandwidths. Therefore, these results are typical of what we should achieve on the sky after optimization of the AO servo bandwidths. Using  $r_0 = 5.0$  cm (from section 4.1.1), a wind velocity of 1 m/s,  $D$  of 1 meter and a wavelength of  $0.5 \mu m$  results in a residual tip/tilt error of 0.0127 arcsecond. This is  $0.06\lambda/D$ , or 22 nm of wavefront error.

#### 4.2.2. High order temporal errors

The RMS phase error (in radians) resulting from the finite control bandwidth of the deformable mirror is given by<sup>9</sup>,

$$\sigma_{Temporal\_DM} = \left( \frac{f_g}{f_{3dB}} \right)^{\frac{5}{6}} [rad]$$

Where  $f_g$  is the Greenwood frequency, is given by:

$$f_g = \left( \frac{0.427v}{r_0} \right) [Hz]$$

Figure 8 shows the open and closed loop reconstructed phase errors. The PSD is calculated for each subaperture and averaged over all subapertures. Data for the PSD comes from the running the AO system with the DM loops open and closed and recording telemetry at 100Hz. The estimated servo control bandwidth is 10 Hz. As has been noted in the previous section, this value is approximately 10 times lower than the expected value, and is most likely due to non-optimal servo control parameters. As in section 4.2.1, this is offset by the lower wind velocity in the testbed. The calculated Greenwood frequency is 8.58 Hz, which results in 70 nm of wavefront error.

#### 4.3. Atmospheric fitting errors

The atmospheric fitting error refers to the inability of the AO system to correct wavefront errors on spatial scales smaller than approximately  $2*d$ , where  $d$  is the spacing between actuators at the primary mirror (10 cm in our testbed). The fitting error from a continuous face sheet DM is given by<sup>10</sup>:

$$\sigma_{Atm\_Fitting} = 0.49 \left( \frac{d}{r_0} \right)^{\frac{5}{6}} [rad]$$

This results in an error of 70 nm given the measured  $r_0$  value of 5.0 cm.

#### 4.4. Calibration

The Shack-Hartmann wavefront sensor detects aberrations in optical path of the sensing 635-nm wavelength but does not measure wavefront errors in the non-common optical path of the communications system. See Figure 1 showing the schematic of the optical path. Correspondingly, any aberrations in the WFS are non-common path and degrade the quality of the wavefront in the communications path. In order to optimize the performance of the AO system, these errors need to be taken into account. Hence rather than driving the images of the beacon on the 20X20 subapertures to


the centers of the corresponding 2X2 quad cells, centroids are driven to an offset value to produce an optimized wavefront in the communications path.

The first step in the calibration is to determine the DM shape that maximizes Strehl in the communications path. An application was written that allowed arbitrary Zernike<sup>11</sup> modes to be applied to the DM. Beginning with the low order terms, each Zernike mode is adjusted individually to optimize Strehl before continuing to the next mode. The first three Zernike modes (piston, tip, and tilt) remain zero, since piston does not change the shape of the DM, and tip/tilt correction is done using the steering mirror, rather than the DM. Once the optimal coefficients are determined, the process continues with the next Zernike mode. The first 15 Zernike modes were examined using this method. After the optimal DM shape is determined, the centroid values in the WFS are recorded and used as the desired centroid values in the future.

Our results indicate that the wavefront error in the communications path is a function of the zoom (see Figure 4). We used the above method, to determine the first 15 Zernike coefficients at a zoom setting of 5. Before calibration, the imaging camera routinely measured ~39% Strehl. After applying the above correction to the DM, the AO system consistently achieved Strehl ratios of 47% or higher. {This implies that the residual WFE is  $> 1$  radian square across the aperture, or that the effective aperture diameter in the testbed is greater than  $r_0$ , recall the expression for Strehl and the expression for  $r_0$ .} The same procedure was used at a zoom setting of 2, but no significant improvement could be made from the optimal settings determined for a zoom of 5. The optimal DM shape produced a Strehl of 28%. One theory is that changing the zoom lens introduces wavefront aberrations. In this case, one would expect these to be low order aberrations which could be tuned out using the above procedure. However, even after calibration, the Strehl from the zooms of 2 and 5 are significantly different, suggesting that the problem is due to another cause other than wavefront aberrations introduced from changing the zoom. The difference in wavefront error as a function of zoom may be due to scattered light or another related optical alignment problem. We plan to investigate this in the future.

#### 4.5. Comparison of predicted performance to experimental results

Error terms calculated in the above section are added in quadrature and displayed in Table 2. The total predicted wavefront error of 210 nm appears to match the measured value (Section 3.1) of 210 nm. However, this is not a very strong test as the dominant error term is the calibration error (184 nm) which is always a measured value. Ignoring the calibration error, the predicted RMS wavefront error is 101 nm as compared with the measured value (section 3.1) of 102 nm. These values are in very good agreement. The current system is limited by both atmospheric fitting error and temporal delay in updating the DM. Assuming we increase the system bandwidth to the predicted values (approximately 10 times better) and that the atmospheric wind velocities are of the order 10-15 m/s (versus the 1m/s in the experiment), the DM temporal error will not change and the system on the sky will continue to be dominated by these two error terms.

Error Term	Predicted RMS Wavefront Error (nm)	Measured RMS Wavefront Error (nm)
Atmospheric fitting	70	NA
DM Temporal	70	NA
Tip/Tilt Temporal	22	NA
Sub-Total Error	<b>101</b>	<b>102</b>
Calibration (zoom=5)	184	
Total Error	<b>210</b>	<b>210</b>

**Table 2. Predicted and measured AO system performance. The predicted wavefront error of 101 nm agrees very well with the measured value of 102 nm. There is an additional 184 nm of calibration error, which was only determined experimentally.**

## 5. CONCLUSIONS AND FUTURE WORK

We have designed and built an adaptive optics testbed for optical communication, and have shown that the measured performance of the system agrees with theoretical performance predicted by analytical equations. Furthermore, the system performance is limited by calibration of the non-common path. Excluding calibration errors, the system achieves 102 nm RMS of wavefront error. This increases to 210 nm when calibration errors are included.

In the future we plan to improve the turbulence generator to simulate correctly the magnitude of wind velocity expected from the atmosphere. We will also optimize the servo loops to obtain a higher closed loop bandwidth. In order to better understand the system performance we plan to calibrate the WFS, FSM and reconstructor. This will enable direct measurement of the tip/tilt bandwidth, DM bandwidth and WFS measurement errors from telemetry data. These values can then be compared to the analytical values to better understand and validate the system performance.

## ACKNOWLEDGMENTS

This work was carried out at the Jet Propulsion Laboratory, California Institute of Technology under contract with the National Aeronautics and Space Administration and sponsored by the Research and Technology Development program.

## REFERENCES

1. R. DuVarney, C. Bleau, G. Motter, S. Shaklan, A. Kunhnert, G. Brack, D. Palmer, M. Troy, T. Kieu, R. Dekany, "EEV CCD39 wavefront sensor cameras for AO and interferometry," in *Advanced Optical Systems Technology*, P. Wizinowich, ed., Proc SPIE **4007**, 481-492 (2000).
2. T. Truong, G. Brack, M. Troy, T. Trinh, F. Shi, R. Dekany, "real-time wavefront processor for the next generation of adaptive optics systems: a design and analysis," in *Adaptive Optical System Technologies II*, P. Wizinowich, D. Bonaccini, eds., Proc SPIE **4839**, 911-922 (2003).
3. M. Wright, M. Srinivasan, K. Wilson, "improved optical communications performance using adaptive optics with an avalanche photodiode detector," JPL IPN progress report, to be published, Feb., 2005
4. A. Marechal, *Rev. d'Optique* **26**, 257 (1947)
5. D. Fried, "Optical resolution through a randomly inhomogeneous medium for very long and very short exposures," *J. Opt. Soc. Am.* **56**, 1372-1379 (1966).
6. K. Wilson, A. Vaughan, J. Wu, D. Mayes, J. Maloney, R. Sobek, "preliminary characterization results of the OCTL telescope," JPL IPN progress report, to be published, Feb., 2005
7. J. Hardy, *Adaptive Optics for Astronomical Telescopes*, pp. 87-88. Oxford Univ. Press, New York, 1<sup>st</sup> ed., (1998).
8. G. Tyler, Report TR-887, The Optical Sciences Co. (1988)
9. J. Hardy, *Adaptive Optics for Astronomical Telescopes*, pp. 337-338. Oxford Univ. Press, New York, 1<sup>st</sup> ed., (1998).
10. J. Hardy, *Adaptive Optics for Astronomical Telescopes*, pp. 342-343. Oxford Univ. Press, New York, 1<sup>st</sup> ed., (1998).
11. J. Hardy, *Adaptive Optics for Astronomical Telescopes*, pp. 95-96. Oxford Univ. Press, New York, 1<sup>st</sup> ed., (1998).

# FIGURES

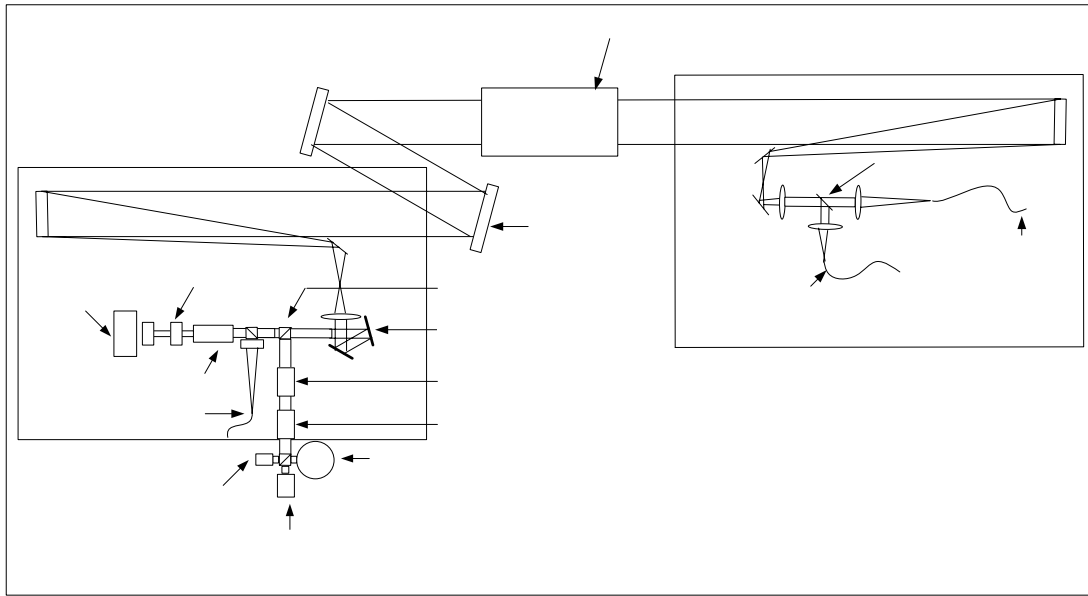


**Figure 1. Optical layout of the AO optical communication testbed.**

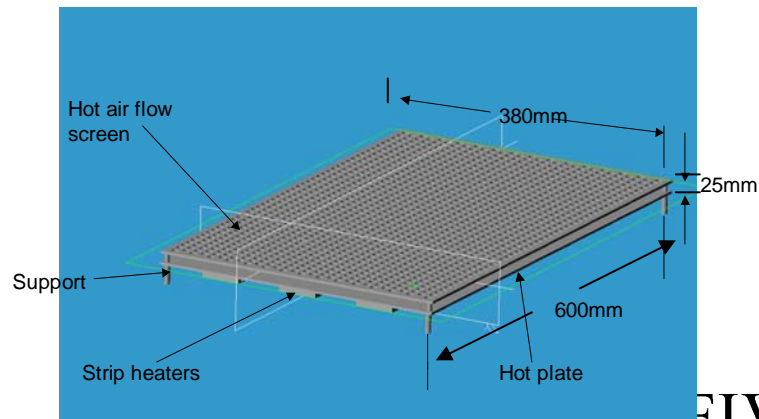


**Figure 2. Physical dimensions of the turbulence generator used in the testbed.**

RECEIVER

Lenslet Array

WFS CCD

Beam Compressor



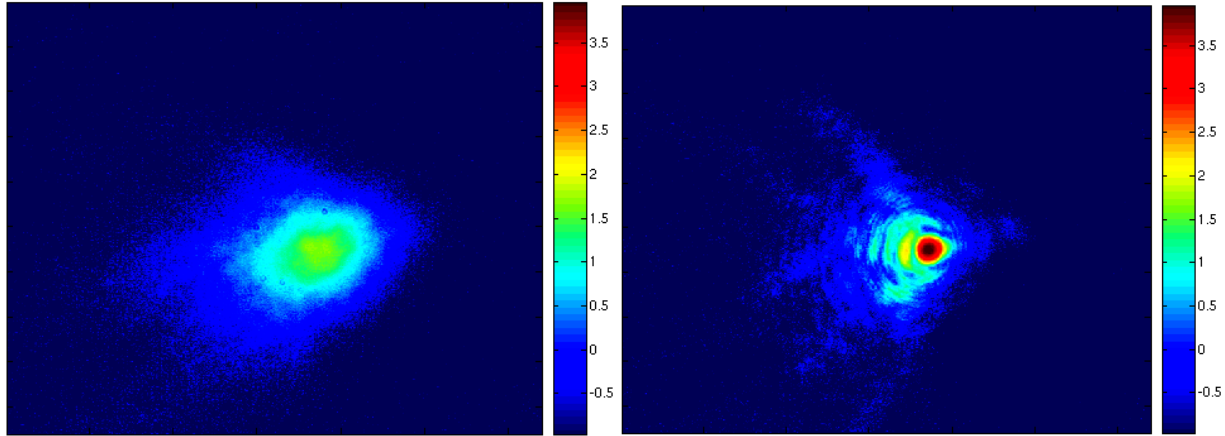


**Figure 3. Open (left) and closed (right) loop images with the turbulence generator turned on. The open loop image has a FWHM of 1428  $\mu\text{m}$  or 5.8  $\lambda/\text{D}$ . The closed loop image has a FWHM of 246  $\mu\text{m}$  or 1  $\lambda/\text{D}$ . Data was taken at zoom setting of four.**

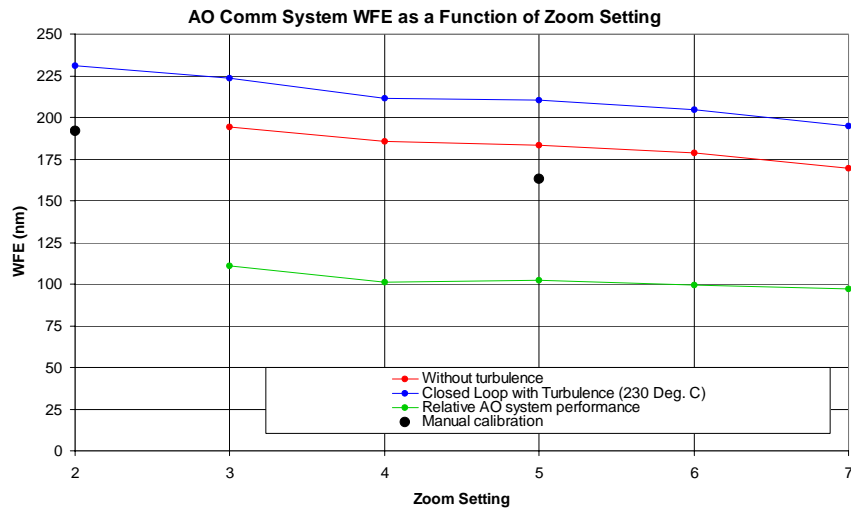


**Figure 4. RMS Wavefront error vs. zoom setting with the turbulence generator turned on and off. Also plotted is the relative AO system performance which is defined as the subtraction (in quadrature) of the turbulence on and off results.**

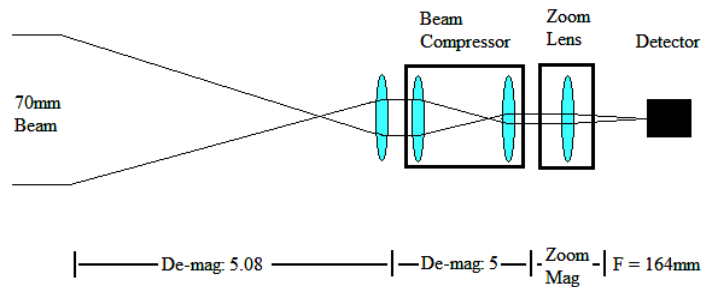


**Figure 5. Simplified layout of 1.064  $\mu\text{m}$  optical path**

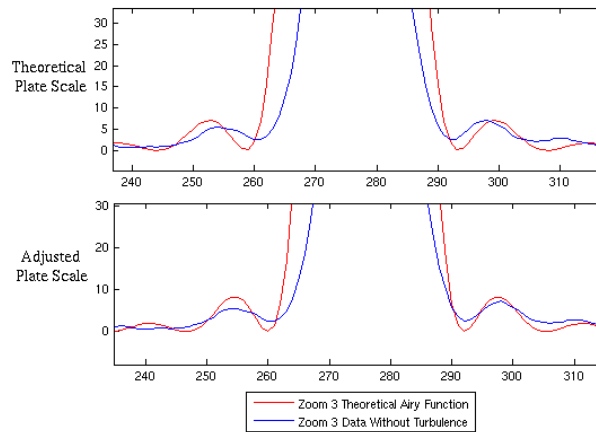


**Figure 6. Comparison of measured data with generated Airy image. The plate scale was adjusted by 8% so that the zeros of the airy function agreed with the measured data.**

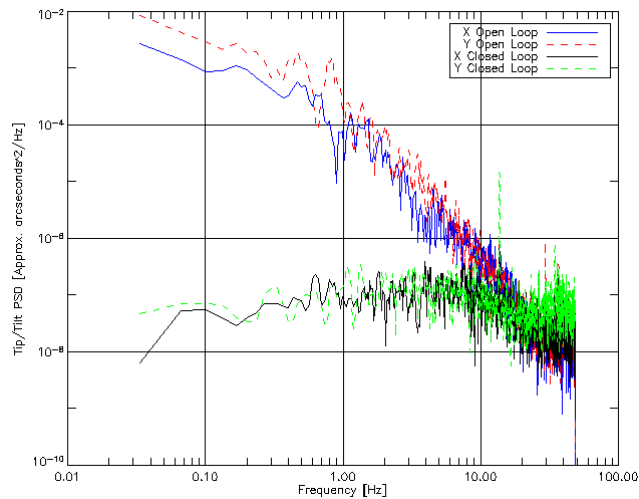


**Figure 7. The open and closed loop tip/tilt PSD with the turbulence generator turned on. The servo bandwidth is estimated to be about 10 Hz and the wind velocity is  $\sim 1$  m/s.**

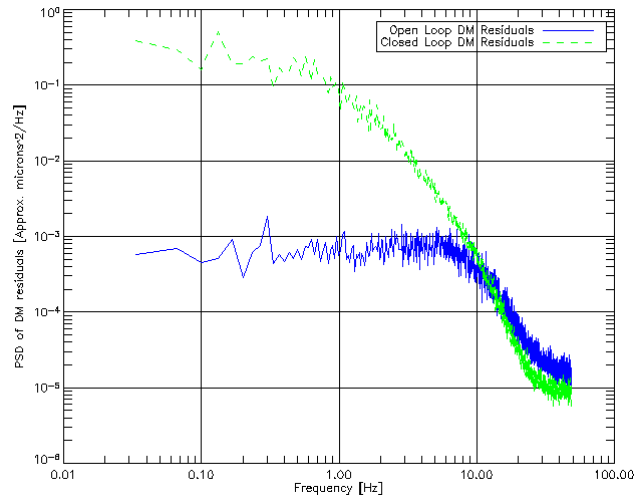


**Figure 8. The PSD of the open and closed loop DM residuals with the turbulence generator on. The PSDs were calculated for each DM actuator and averaged. The servo bandwidth is about 10Hz.**